Photonic band gaps in quasiperiodic photonic crystals with negative refractive index

M. S. Vasconcelos,[1] P. W. Mauriz,[1] F. F. de Medeiros,[2] and E. L. Albuquerque[2]

[1]*Departamento de Ciências Exatas, Centro Federal de Educação Tecnológica do Maranhão, 65025-001 São Luís, Maranhão, Brazil*
[2]*Departamento de Física, Universidade Federal do Rio Grande do Norte, 59072-970 Natal, Rio Grande do Norte, Brazil*

We investigate the photonic band gaps in quasiperiodic photonic crystals made up of both positive (SiO_2) and negative refractive index materials using a theoretical model based on a transfer matrix treatment. The quasiperiodic structures are characterized by the nature of their Fourier spectrum, which can be dense pure point (Fibonacci sequences) or singular continuous (Thue-Morse and double-period sequences). These substitutional sequences are described in terms of a series of generations that obey peculiar recursion relations. We discussed the photonic band gap spectra for both the ideal cases, where the negative refractive index material can be approximated as a constant in the frequency range considered, as well as the more realistic case, taking into account the frequency-dependent electric permittivity ϵ and magnetic permeability μ. We also present a quantitative analysis of the results, pointing out the distribution of the allowed photonic bandwidths for high generations, which gives a good insight about their localization and power laws.

I. INTRODUCTION

Materials with simultaneously negative permittivity ϵ and negative permeability μ, yielding a negative refractive index η (i.e., the negative square root $\eta = \sqrt{\epsilon\mu}$ had to be chosen), have recently been extensively studied in several distinct artificial physical settings, inspired by Veselago's work[1] many years ago. Veselago coined these peculiar materials as left-handed materials, because they support backward waves (their energy and phase velocity are antiparallel),[2] for which the electric field $\vec{E}$, the magnetic field $\vec{H}$, and the wave vector $\vec{k}$ form a left-handed set of vectors (the Poynting vector $\vec{S}$ is antiparallel to the wave vector; for an up to date review, see Ref. 3).

Left-handed materials exhibit new electromagnetic response functions which cannot be found in nature. Actually, this class of material, which we shall refer to as *metamaterials*, does not need to be a homogeneous piece of matter. On the contrary, it could acquire their electromagnetic properties from small structures, whose collective behavior is impossible to obtain from its constituents. To be more specific, the non-natural electromagnetic response means that the refraction index in these materials is negative. They can be artificially fabricated with periodic metallic structures,[4–6] whose length of the period is smaller than the wavelength at which the unusual properties occur. In the optical domain, these materials should have dimensions in the micrometer range or less, and they can be fabricated easily in the microwave region.[7–9] Besides, the anomalous refraction at the boundary between a negative refractive index material and a conventional medium, with positive refractive index, can lead to exciting features that can be advantageous in the design of novel devices and components. Indeed, these engineered metamaterials will offer creative solutions in the development of new electromagnetic devices, such as multifunctional antennas and embedded sensors suitable for various applications in wireless and optical systems.[10]

An alternative approach in attaining negative refraction uses the properties of *photonic crystals*, structured materials with a periodic dielectric constant, whose optical band structure is analogous to the electronic band structure in a solid.[11–13] Their characteristic band structure and surface waves have been extensively studied by using a transfer matrix formalism.[14,15] Finite periodic system of alternating dielectric layers bounded by air was also investigated,[16] in which the surface modes of each boundary can interact and become coupled in a variable degree depending on both the truncation of the outer layers and the total thickness of the crystal slab. More recently, the characteristics of multilayers incorporating left-handed materials have attracted many researchers. Of particular interest is the scaling behavior of the band gap around the frequency where the average index of refraction of the multilayer structure vanishes, the so-called zero-$\bar{\eta}$ photonic region, which was later associated with omnireflective properties.[17] However, subsequent studies demonstrated that this behavior is not universally true,[18] giving rise to subsequent research works to explore the possibility of surface waves on the interface of such multilayer structures (see, for instance, recent results of Namdar *et al.*[19]). Besides, the existence of photonic superlattices of null gap with band-touching phenomena was demonstrated, indicating the importance of one-dimensional photonic superlattices for many important practical applications[20] such as a superlens device which can occur in a simple slab of this material, with an image construction that follows precisely the simple rules of geometric optics.[2]

When the electromagnetic radiation propagating through a polarizable dielectric or magnetic crystal excites some internal degrees of freedom of the crystal, it gives rise to a hybrid (or mixed) modes called polaritons. Polaritons are quasiparticles consisting of a photon coupled to an elementary excitation (plasmon, phonon, exciton, etc.) which polarizes the crystal. The theory of polariton in conventional bulk materials is well known (see, e.g., Refs. 21–23). Specifically, in the case of an electron plasma, such excitation will have both a photon and a plasmon component, because the total energy is distributed over the whole system due to the coupling. The resultant mode, the plasmon-polariton, may have either a

very strong photon or a very strong plasmon component, or may be strongly mixed, depending on the wave vector. A similar definition could be used by other types of polaritons. Experimental evidences for these excitations were probed first by Henry and Hopfield[24] and, nowadays, they have been turned important in applied solid state physics, especially at nanometer scale. For example, the effect of surface plasmon-polaritons in nanoslit array, where the light is refracted and transmitted forming "nanolens," have been proposed recently[25] based on finite-difference time-domain numerical simulation. In the nanolens, the light incident wave excites a surface plasmon-polariton mode at the slit entrance, which afterward propagates along the slit region with a complex propagation constant and decouples into radiation modes at the slit exit, diffracting into all radial directions with a uniform power distribution.

Polaritons in quasiperiodic structures exhibit collective properties not shared by their constituents. Therefore, the long-range correlations induced by the construction of these systems are expected to be reflected someway in their spectra, defining a novel description of disorder. Indeed, theoretical transfer matrix treatments show that these spectra are fractals (for an up to date review of this subject, see Ref. 26). The study of the fractal spectra generated by these quasiperiodic structure can help us understand the global order and the rules that these systems obey at high generation order.

The aim of this work is twofold: first, we want to show the photonic band gap spectra, which arise from the propagation of a plasmon-polariton excitation in quasiperiodic multilayer structure comprised of alternating layers of both positive (SiO_2) and negative refractive index materials using a theoretical model based on a transfer matrix treatment. The quasiperiodic structures follow the Fibonacci (FB), Thue-Morse (TM) and double-period (DP) substitutional sequences and can be generated by the following inflation rules: $A \rightarrow AB$, $B \rightarrow A$ (FB); $A \rightarrow AB$, $B \rightarrow BA$ (TM); and $A \rightarrow AB$, $B \rightarrow AA$ (DP), where A and B are the building blocks modeling the metamaterial and SiO_2, respectively. We make use of the transfer matrix approach to analyze them, simplifying the algebra which would be otherwise quite involved (for more details, see Ref. 27). Second, we intend to present a quantitative analysis of the results, pointing out the distribution of the allowed photonic bandwidths for high generations, which gives a good insight about their localization and power laws.

The plan of this work is as follows. In Sec. II, we present the method of calculation employed here, which is based on the transfer matrix approach. The plasmon-polariton dispersion relation (bulk and surface modes) is then determined. Section III is devoted to the discussion of this dispersion relation for the periodic and quasiperiodic structures. Further, we also present their localization profiles and the connection with a fractal and/or multifractal behavior through the scaling law of their bandwidth spectra, as well as the $f(\alpha)$ curve which characterizes a multifractal profile. The conclusions of this work are presented in Sec. IV.

II. GENERAL THEORY

A schematic illustration of an infinite periodic photonic superlattice (the periodic case is nothing but the second gen-
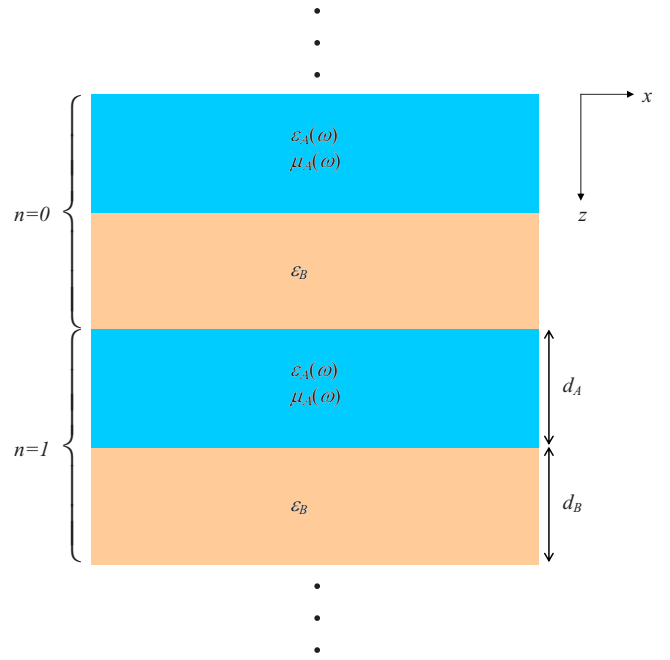

FIG. 1. (Color online) The schematic representation of the photonic superlattice, whose unit cell has a size $L = d_A + d_B$. [The blue (brown) layer corresponds to material A (B).]

eration of the Fibonacci sequence) consisting of alternating layers $\cdots ABABA \cdots$ is shown in Fig. 1. Here, medium A (metamaterial) has thickness d_A, while medium B (SiO_2) has thickness d_B. Neglecting any damping term (when losses of the metamaterial are considered, the damping factor can be defined as a fraction of the plasma frequency), the metamaterial possesses the negative refractive index in the microwave region, whose corresponding dielectric permittivity $\epsilon_A(\omega)$ and magnetic permeability $\mu_A(\omega)$ are, respectively, given by[28]

$$\epsilon_A(\omega) = 1 - \omega_p^2/\omega^2, \tag{1}$$

$$\mu_A(\omega) = 1 - F\omega^2/(\omega^2 - \omega_0^2), \tag{2}$$

where the plasma frequency ω_p, the resonance frequency ω_0, and the fraction F are determined only by the geometry of the lattice rather than by the charge, effective mass, and density of electrons. The physical parameters used here are $\omega_0/2\pi = 4$ GHz, $\omega_p/2\pi = 10$ GHz, and $F = 0.56$, motivated by the experimental work of Smith *et al.*[7] It is easy to see that for $\omega_0 < \omega < 0.6\omega_p$, both the dielectric permittivity $\epsilon_A(\omega)$ and magnetic permeability $\mu_A(\omega)$ are negative.

The bulk plasmon-polariton dispersion relation of the periodic superlattice is obtained by solving the electromagnetic wave equation for p-polarized electromagnetic mode within the layers A and B of the nth unit cell of the superlattice. So, we can easily deduce that the components of the electric and magnetic fields within the layer $j = A$ or B of the nth unit cell have the form

$$E_{xj}(z) = A_{1j}^n \exp(-k_{zj}z) + A_{2j}^n \exp(k_{zj}z), \tag{3}$$

$$E_{zj}(z) = (ik_x/k_{zj})[A_{1j}^n \exp(-k_{zj}z) - A_{2j}^n \exp(k_{zj}z)], \quad (4)$$

$$H_{yj}(z) = [-i\omega\epsilon_j(\omega)/k_{zj}][A_{1j}^n \exp(-k_{zj}z) - A_{2j}^n \exp(k_{zj}z)], \quad (5)$$

$$k_{zj} = \begin{cases} [k_x^2 - \epsilon_j\mu_j(\omega)\omega^2/c^2]^{1/2} & \text{if } k_x > (\epsilon_j\mu_j)^{1/2}(\omega/c) \\ i[\epsilon_j\mu_j(\omega)\omega^2/c^2 - k_x^2]^{1/2} & \text{if } k_x < (\epsilon_j\mu_j)^{1/2}(\omega/c). \end{cases} \quad (6)$$

Here, k_x is the common in-plane wave vector, ω is the angular frequency, and c is the velocity of light in vacuum. The appropriate electromagnetic fields for p-polarized waves are given by

$$\vec{E}_j(x,z,t) = (E_{xj},0,E_{zj})\exp(ik_xx - i\omega t), \quad (7)$$

$$\vec{H}_j(x,z,t) = (0,H_{yj},0)\exp(ik_xx - i\omega t). \quad (8)$$

Then, employing the standard electromagnetic boundary conditions at the interfaces of the unit cell, we can find the appropriate (unimodular) transfer matrix for the periodic superlattice as

$$|A_A^{n+1}\rangle = T|A_A^n\rangle, \quad T = N_A^{-1}M_A N_B^{-1}M_B, \quad (9)$$

and

$$|A_j^n\rangle = \begin{bmatrix} A_{1j}^n \\ A_{2j}^n \end{bmatrix}. \quad (10)$$

This transfer matrix T relates the electromagnetic field amplitudes of a layer in cell n to the equivalent one in cell $n \pm 1$. Here, M_j and N_j ($j = A$ or B) are given by

$$M_j = \begin{pmatrix} f_j & \bar{f}_j \\ f_j/(Z_j \cos \theta_j) & -\bar{f}_j/(Z_j \cos \theta_j) \end{pmatrix}, \quad (11)$$

$$N_j = \begin{pmatrix} 1 & 1 \\ 1/(Z_j \cos \theta_j) & -1/(Z_j \cos \theta_j) \end{pmatrix}. \quad (12)$$

Here, $Z_j = \sqrt{\mu_j/\epsilon_j}$ is the impedance of medium j, and $\sin(\theta_j) = \eta_j(\omega/c)/k_x$. Also,

$$f_j = \exp(-k_{zj}d_j), \quad \xi_j = \epsilon_j(\omega)/k_{zj}, \quad \bar{f}_j = 1/f_j, \quad (13)$$

with d_A and d_B being the thickness of layers A and B, respectively.

Now, using the Floquet-Bloch ansatz, we obtain the dispersion relation for the bulk plasmon-polariton modes in the form

$$\cos(QL) = (1/2)\text{Tr}(T), \quad (14)$$

where $\text{Tr}(T)$ means the trace of the transfer matrix T. Using Eqs. (9)–(12), we have

$$\cos(QL) = \cos(k_{zA}d_A)\cos(k_{zB}d_B) - f(\omega)\sin(k_{zA}d_A)\sin(k_{zB}d_B), \quad (15)$$

where

$$f(\omega) = \frac{1}{2}\left[\frac{Z_A \cos(k_{zA}d_A)}{Z_B \cos(k_{zB}d_B)} + \frac{Z_B \cos(k_{zB}d_B)}{Z_A \cos(k_{zA}d_A)} \right], \quad (16)$$

with Q being the Floquet-Bloch wave vector.

To set up the dispersion relation for the surface plasmon-polariton modes, we consider a superlattice truncated at $z = 0$ with the region $z < 0$ filled by a transparent medium C, whose frequency-independent dielectric constant is denoted by ϵ_C. This semi-infinite superlattice does not possess full translational symmetry in the z direction through multiples of the unit cell thickness L, and therefore, Bloch theorem is not anymore valid, as in the bulk case. However, Eq. (14) still holds provided we replace Q by the complex quantity $i\beta$, with β being an attenuation factor,[29,30] yielding

$$\cosh(\beta L) = (1/2)\text{Tr}(T). \quad (17)$$

Since we now have to consider the extra boundary condition for the new interface at $z = 0$, this imposes a further constraint which enables us eventually to determine the attenuation factor β. The relevant electromagnetic fields in the region $z < 0$ have the form

$$E_x(z) = C^0 \exp(k_{zC}), \quad (18)$$

$$H_y(z) = (i\omega\epsilon_C/k_{zC})C^0 \exp(k_{zC}), \quad (19)$$

where C^0 is a constant and $k_{zC} = [k_x^2 - \epsilon_C\omega^2/c^2]^{1/2}$, for $k_x > \epsilon_C^{1/2}\omega/c$. Applying the boundary conditions at $z = 0$, we have

$$C^0 = A_{1A}^0 + A_{2A}^0, \quad (20)$$

$$\xi_C C^0 = \xi_A(A_{1A}^0 - A_{2A}^0), \quad (21)$$

where $\xi_C = \epsilon_C/k_{zC}$. Therefore, for the interfaces, we have

$$T|A_A^0\rangle = \exp(-\beta L)|A_A^0\rangle, \quad (22)$$

where

$$|A_A^0\rangle = \begin{bmatrix} A_{1A}^0 \\ A_{2A}^0 \end{bmatrix}. \quad (23)$$

Eliminating the unknown coefficients C, A_{1A}^0, and A_{2A}^0 from Eqs. (20) and (21), we obtain

$$T_{11} + T_{12}\lambda = T_{22} + T_{21}\lambda^{-1}, \quad (24)$$

were T_{ij} ($i,j = 1,2$) are the elements of the transfer matrix T, and λ is a surface dependent parameter given by

$$\lambda = (\xi_A + \xi_C)/(\xi_A - \xi_C), \quad (25)$$

$$\xi_j = \epsilon_j(\omega)/k_{zj}. \quad (26)$$

Here, ϵ_j is the dielectric function of the medium under consideration (A or C). Equation (24) represents an implicit dispersion relation for the surface plasmon-polariton modes. Once it is solved, we can obtain a value for β which must satisfy Eq. (17) together with the requirement $\text{Re}(\beta) > 0$ to ensure the localization.

This method can now be extended to a more complex quasiperiodic structure by determining the appropriated

transfer matrices. For instance, it is straightforward to prove that the transfer matrices for any Fibonacci k generation (with $k \geq 1$) is[31]

$$T_{S_{k+2}} = T_{S_k} T_{S_{k+1}}, \qquad (27)$$

with the initial conditions

$$T_{S_0} = N_B^{-1} M_B, \quad T_{S_1} = N_A^{-1} M_A. \qquad (28)$$

Therefore, from the knowledge of the transfer matrices T_{S_0} and T_{S_1}, we can determine the transfer matrix of any other Fibonacci generation. In a similar way, we can find the transfer matrices for all the other quasiperiodic structures (for details, see Ref. 31).

III. NUMERICAL RESULTS

In this section, we present some numerical results to characterize the photonic band gap spectra due to the plasmon-polariton excitation (bulk and surface modes) that can propagate in the structures considered here. We consider medium B as SiO$_2$, with $\epsilon_B = 12.3$ and $\mu_B = 1$, which are the parameters appropriated for this material, while for medium A (metamaterial), we have the frequency-dependent dielectric function $\epsilon(\omega)$ and magnetic permeability $\mu(\omega)$ given by Eqs. (1) and (2), respectively.

The photonic band gap spectrum for the periodic superlattice is depicted in different scales from Figs. 2(a)–2(c). In all these figures, the surface modes are represented by straight lines, while the bulk bands are characterized by the shadow areas, which are limited by the equations $QL = 0$ and $QL = \pi$. The dashed line represents the light line $\omega = ck_x$ in the vacuum, while the chain-dotted line is the light line $\omega = ck_x/\epsilon_B^{1/2}$ in the positive refractive index material SiO$_2$. As it was already mentioned before, the damping is neglected and we assume the external medium C to be vacuum ($\epsilon_C = 1$), yielding the structure vacuum/metamaterial/SiO$_2$/metamaterial/SiO$_2$···.

In Fig. 2(a), the photonic band gap frequency (in units of the plasma frequency) is plotted against the dimensionless in-plane wave vector $k_x d_A$ for $d_A/d_B = 2$ with $d_A = 8$ mm. The polariton spectrum has three well-defined bulk frequency branches, separated by forbidden frequency gaps where the surface modes can propagate. For low frequencies, the bulk branches become narrower when $k_x d_A$ increases. They tend (together with the lower surface mode) asymptotically to the limit value $\omega/\omega_p = 0.276$. The high-frequency branch have a parabolic form such as the plasmon-polariton dispersion relation presented in positive refractive index materials. Observe that the middle frequency branch, localized in the frequency range $0.276 \leq \omega/\omega_p \leq 1.0$, has a negative slope in the bulk modes, characterizing a negative group velocity for these modes. On the other hand, there are two surface modes in Fig. 2(a): the one in the high-frequency region, whose slope is negative in all intervals, is the so-called backward mode, starting at the light line $\omega = ck_x$ and tending to $\omega/\omega_p = 1/\sqrt{2}$ for high value of $k_x d_A$. The other one lies at the low-frequency region, whose slope is initially positive (forward mode), starting on $\omega/\omega_p = 0$ and $k_x d_A = 0$ and tending to
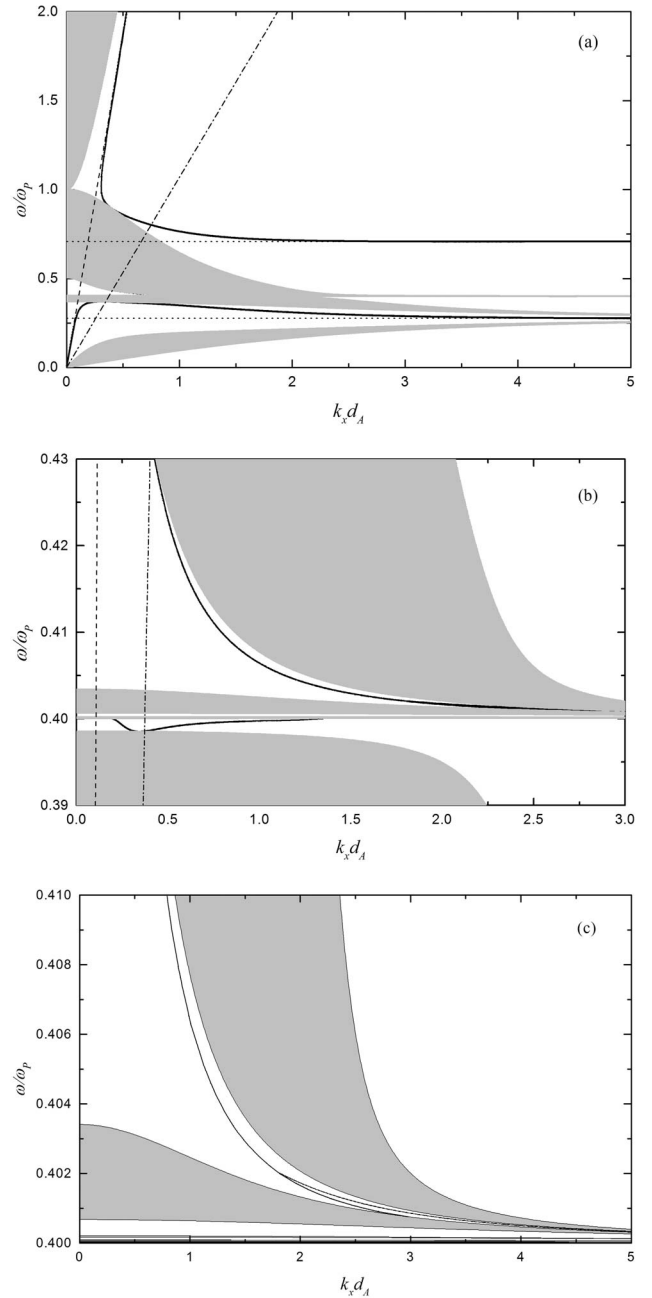

FIG. 2. Photonic band gap frequency spectrum, as given by Eq. (14) (bulk modes) and Eq. (24) (surface modes), for a periodic photonic superlattice. The shaded areas represent the three bulk mode regions, while the surface modes are represented by full lines. The dashed line represents the light line in the vacuum, while the chain-dotted line is the light line in layer B (SiO$_2$). In (a), the frequency (in units of the plasma frequency) is plotted against the dimensionless in-plane wave vector $k_x d_A$, considering the thickness ratio $d_A/d_B = 2$. In (b), we have plotted an amplification of (a) for the region $0.39 \leq \omega/\omega_p \leq 0.43$. In (c), we show a zoom in the region $0.40 \leq \omega/\omega_p \leq 0.41$ of (b).

$\omega/\omega_p = 0.276$ for high values of $k_x d_A$, with negative slope (backward mode).

In order to investigate in more detail the surface modes, we have showed in Fig. 2(b) a zoom in the photonic band gap spectra depicted in Fig. 2(a) for the region 0.39

$\leq \omega/\omega_p \leq 0.43$. Two more surface modes arise; the first one, a degenerate surface mode (with the same value for ω and two different values for $k_x d_A$), emerges from one bulk band at $\omega/\omega_p = 0.4$ and $k_x d_A = 0.194$ and converges for the same bulk band at $k_x d_A = 1.275$. Its inflexion point intercepts a lower bulk band at $k_x d_A = 0.377$. In this case, we have a backward surface mode which extends from $k_x d_A = 0.194$ to 0.337 and a forward surface mode which extends from $k_x d_A = 0.337$ to 1.275. The second one emerges from the upper bulk band with negative slope (backward mode) and tends asymptotically to the limit value $\omega/\omega_p = 0.4002$ when $k_x d_A$ increases. In Fig. 2(c), the characteristics of this second mode can be better observed. It divides at $k_x d_A = 1.733$, with the upper branch converging to one bulk band and the lower branch converging to the other one. In all cases, for the forward surface modes, the direction of the total energy flow coincides with the propagation direction, while for the backward modes, the energy flow is backward with respect to the in-plane wave vector $k_x d_A$. A similar behavior for the degenerate surface mode, shown in Fig. 2(b), was founded by Namdar et al.[19] More important, the bifurcation of the surface mode shown in Fig. 2(c), which appears in the frequency region where the metamaterials have a negative refractive index, is another feature of the photonic band gap spectra. A comparison of the spectrum depicted in Fig. 2(c) with those presented in a previous work,[27] for one-dimensional periodic structures with the metamaterial substituted by a corresponding positive index medium (GaAs), strongly suggests that the bifurcation of the surface mode has its origin linked to the left-handed properties of one of the constituent building block layers (the metamaterial medium A). Besides, photonic band gaps in Thue-Morse aperiodic systems with both constituents as positive index media also did not show a similar behavior, although for this case, the spectra can be neatly separated into two flavors, the fractal gaps (which are a consequence of the aperiodic geometry) and the traditional gaps presented in the absence of a fractal structure (as the Thue-Morse one).[32]

In Fig. 3(a), we present the photonic band gap spectrum for the fourth generation of the Fibonacci quasiperiodic structure. Different of the periodic case, the photonic band gap spectrum is more fragmented and tends to become narrower when $k_x d_A$ increases. There are several bulk modes separated by narrow forbidden band gaps, a characteristic due to the quasiperiodic geometry. Observe that the number of passbands, considering both regions of high and low frequency, is related to the Fibonacci number F_n ($F_n = F_{n-1} + F_{n-2}$, starting with $F_1 = F_2 = 1$). We can observe the existence of five surface modes with a behavior similar to those found for the periodic case. The high-frequency surface mode emerges from the light line $\omega = c k_x$ and then goes to $\omega/\omega_p = 1/\sqrt{2}$ for high values of $k_x d_A$, with negative slope. The second, the third, and the fourth surface modes, seen from top to the bottom, alternate negative and positive slopes, showing the forward and backward propagations. The second surface mode emerges from the light line with null slope and it tends to $\omega/\omega_p = 1/\sqrt{2}$ with negative slope (backward mode), together with the bulk bands below and above them. The third surface mode emerges from a thin bulk band at $\omega/\omega_p = 0.4$, with a null slope, and goes to $\omega/\omega_p = 0.276$,
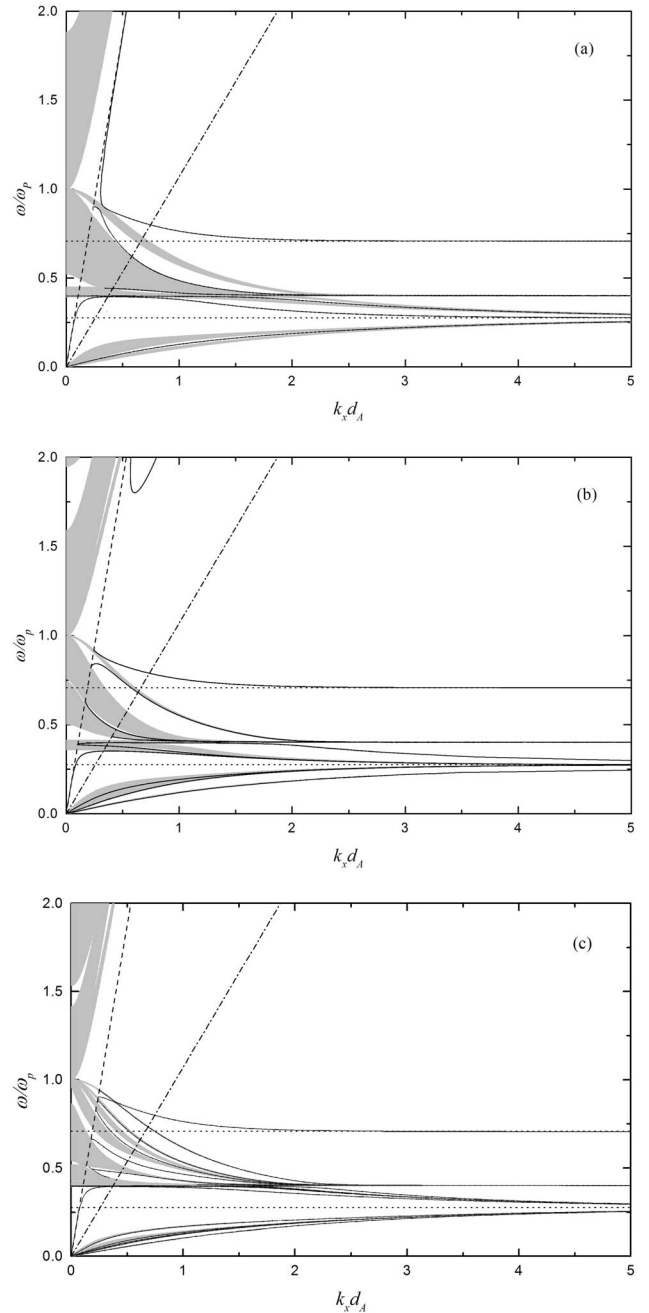

FIG. 3. Photonic band gap spectra (in units of the plasma frequency) against the dimensionless in-plane wave vector $k_x d_A$ for the thickness ratio $d_A/d_B = 2$ considering a quasiperiodic photonic superlattice. The shaded areas represent the bulk mode regions, while the surface modes are represented by full lines. The dashed line represents the light line in the vacuum, while the chain-dotted line is the light line in layer B (SiO$_2$). (a) Fibonacci, (b) Thue-Morse, and (c) double period.

with negative slope. The fourth surface mode starts at $\omega/\omega_p = 0$ and $k_x d_A = 0$ and then tends together with the bulk bands to $\omega/\omega_p = 0.276$ for high values of $k_x d_A$. The fifth and last surface mode begins at $\omega/\omega_p = 0$ and $k_x d_A = 0$ and tend to $\omega/\omega_p = 0.276$, with positive slope in all interval shown in the figure. Therefore, it is a forward wave mode, i.e., in this region, we do not have the effect of the negative refraction

index or, more specifically, we do not have backward modes. As we will see, the behavior of this last surface mode is similar to those found in other quasiperiodic cases, i.e., at low frequencies and between the bulk bands localized in the range $0 \leqslant \omega/\omega_p \leqslant 0.276$, we have only forward modes.

For completeness, we have also shown the fourth generation for the Thue-Morse and double period quasiperiodic structures in Figs. 3(b) and 3(c), respectively. Here, different from the Fibonacci case, we have many passbands that are fragmented and follow a different rule: for both quasiperiodic structures, the number of fragmented bulk regions N increases as $(1/3)[2^n - (-1)^n + 2]$, with n being the Thue-Morse (double-period) generation number. Besides, there are surface modes (straight lines) above, below, and between the bulk bands with the same properties as those in the Fibonacci case, i.e., forward and backward propagations. It is easy to observe that in all these quasiperiodic structures, in the interval $0 \leqslant \omega/\omega_p \leqslant 0.4$, we have the same qualitative behavior for the surface and bulk modes when compared to superlattices composed by positive refractive index materials, while in the range $0.4 \leqslant \omega/\omega_p \leqslant 1.0$, we note the effects of the negative refractive index material. Such fact can be due to the refraction index $\sqrt{\epsilon\mu}$ being negative in the range $0.4 \leqslant \omega/\omega_p \leqslant 0.6$. However, this does not explain all the results observed out of this interval as, for instance, the negative group velocity for the two surface modes at high frequency, depicted in Fig. 3(b). The upper surface mode emerges from the light line and, while $k_x d_A$ increase, it tends asymptotically to the convergence limit in $\omega/\omega_p = 1/\sqrt{2}$ (dotted line). In the range $0.244 \leqslant k_x d_A \leqslant 2.0$, the slope is negative, which means that the mode has a negative group velocity. For $k_x d_A > 2.0$, the slope is null so is the group velocity. Observe that only this surface mode converges for this limit value.

When the constituents of the superlattice are formed by a material with positive refraction index, the passbands in periodic and quasiperiodic structures can be obtained when the absolute value of the right side of Eq. (14) is less than 1 (cf. Ref. 26 for details), which means a real z component k_z of the wave vector. On the other hand, when it is greater than 1, we have a stop band. However, this is not true when the superlattice contains materials with both positive and negative refraction indices (which is the case treated here). Some complex value of k_z can still make the left-hand side of Eq. (14) smaller than 1, and these complex solutions may have physical significance. This can be seen considering the dispersion curves presented in Fig. 4(a), corresponding to a fixed common dimensionless in-plane wave vector $k_x L/2\pi = 0.1$ and a ratio $d_B/d_A = 2.69$. We have plotted here the reduced frequency $\Omega = \omega L/2\pi c$ against the dimensionless Floquet-Bloch wave vector QL for the fifth Fibonacci generation. We also have focus our interest to the case where the average index of refraction of the superlattice vanishes, the so-called zero-$\bar{\eta}$ photonic region, i.e., $\bar{\eta} = (\eta_A d_A + \eta_B d_B)/L = 0$, with $\eta_A = (\epsilon_A \mu_A)^{1/2} = -3.53$ being the refraction index for the metamaterial ($j=A$) and $\eta_B = (\epsilon_B \mu_B)^{1/2} = 2.19$ being the refraction index for SiO_2 ($j=B$), respectively (these parameters correspond to $\epsilon_A = -2.5$, $\mu_A = -5$, $\epsilon_B = 4.8$, $\mu_B = 1$, $d_A/L = 0.271$, and $d_B/L = 0.729$). The reason for that is to distinguish the usual Floquet-Bloch band gaps, depicted in Figs. 2
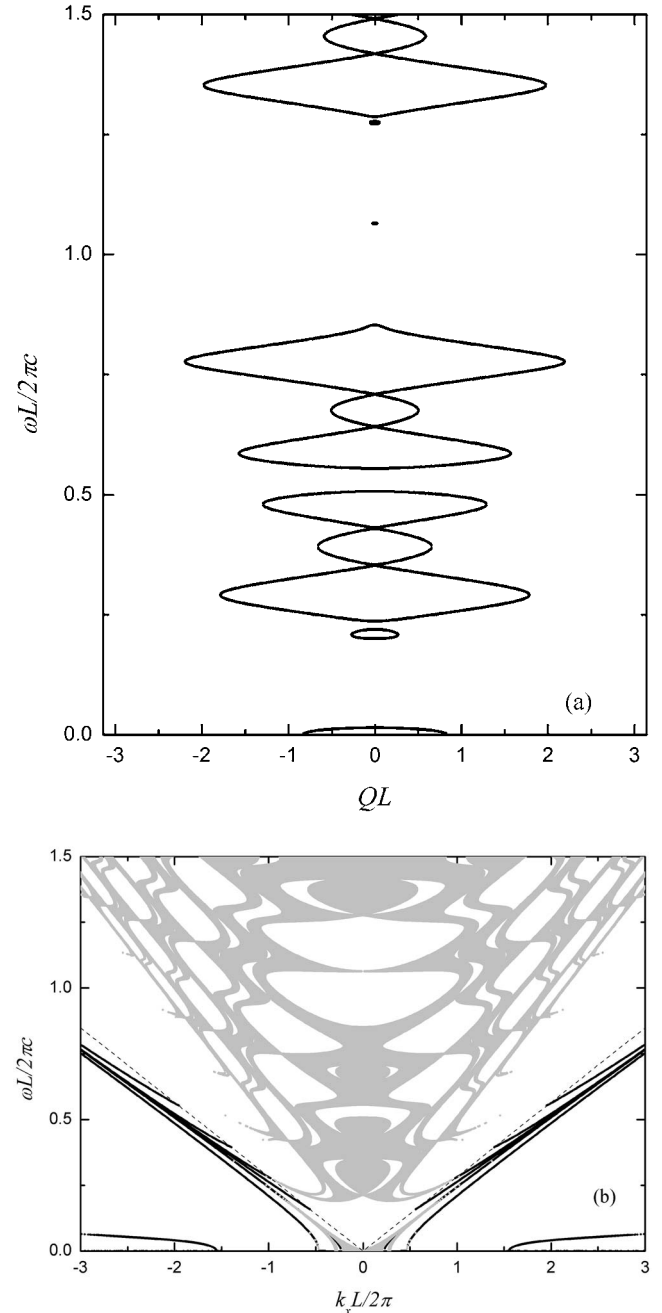

FIG. 4. (a) Photonic band gap spectrum against the dimensionless Floquet-Bloch wave vector QL for the thickness ratio $d_B/d_A = 2.69$, considering the fifth generation of the Fibonacci quasiperiodic photonic superlattice. (b) Projected photonic band structure plotted as a function of the reduced in-plane wave vector $K_x = k_x L/2\pi$. The shaded and the white areas correspond to the passbands and to the stop bands of the structure, respectively. The dashed lines mean the light lines $\omega = ck_x$ and $\omega = -ck_x$ in the vacuum.

and 3, from the zero $\bar{\eta}$ band gaps. Besides, there is a possibility of a gap widening with respect to the usual superlattices constituted only by material with positive refraction index,[33] as well as the possibility of discrete modes and photon tunneling ones[34] when $\bar{\eta} = 0$. Here, we note that the edges

of the bulk bands are not characterized by the Floquet-Bloch conditions $QL=0$ and $QL=\pi$. Therefore, we have a reduction of the Brillouin zone.

The $\bar{\eta}=0$ band structure can be better seen in the projected band profile [Fig. 4(b)] where the consecutive passbands are united to constitute a very large fragmented band, where we can observe discrete and continuous bulk modes. The surface modes are represented by straight lines, and the dashed lines are the light lines corresponding to $\omega=ck_x$ and $\omega=-ck_x$. As we have mentioned, the surface modes lies above the light line and between the bulk bands. When it departs from $k_x=0$, the passbands become separated by narrow stop bands, i.e., the discrete modes transform into narrow bands in which the dimensionless Floquet-Bloch wave vector QL describes a small regions (shadow areas) around $k_x=0$, whereas the lowest dispersion curve extends over a more or less spread domain of the reduced Brillouin zone [see Fig. 4(a)]. On the other hand, Fig. 4(a) also shows that for small values of $k_x d_A$, the transmission through the superlattice is zero, except in certain transmission bands and for some values of $QL<\pi$. The discrete frequencies [as in $\Omega=\omega/2\pi c\simeq 1.2$ and $QL=0$, in Fig. 4(a)] are determined by the Fabry-Pérot resonance condition $k_{zA}=m\pi$ ($m=\pm 1,\pm 2,\pm 3,\dots$), where the waves reflected at consecutive interfaces arrive out of phase at the input facet of the superlattice.[35] The continuous bulk bands are characterized by the reduced Brillouin zone, $0\leqslant QL\leqslant \xi$, with ξ being the values where the slope goes to negative infinity in Fig. 4(a). Note that for the nth Fibonacci generation, we can calculate the dimensionless thicknesses d_A/L and d_B/L that satisfy the equation $\bar{\eta}_n=(F_{n-1}\eta_A d_A+F_{n-2}\eta_B d_B)/L=0$, with F_n being the nth generation's Fibonacci number. In general, for any substitutional sequence, we can calculate these parameters trough the equation

$$\bar{\eta}_n = (N_A\eta_A d_A + N_B\eta_B d_B)/L = 0, \quad (29)$$

where N_A (N_B) is the number of building blocks of layer A (B) for a given generation n.

Now, we examine the confinement effects arising from competition between the long-range aperiodic order, induced by the quasiperiodic structure, and the short-range disorder by means of a quantitative analysis of the localization and magnitude of the passband width in the photonic band gap spectra. To do that, we calculate the regions for allowed frequencies (passbands), where $|(1/2)\mathrm{Tr}(T)|\leqslant 1$, as a function of the generation number of the quasiperiodic structure for a fixed value of $k_x d_A=0.25$, as depicted in Fig. 3(a) (Fibonacci sequence), Fig. 3(b) (Thue-Morse sequence), and Fig. 3(c) (double-period sequence). Such a result can be seen in Figs. 5–7 together with a log-log plot of the total bandwidth as a function of the number of building blocks for each quasiperiodic superlattice, considering three values of $k_x d_A$, namely, 0.25, 0.35, and 0.5, respectively.

Figure 5(a) shows the distribution of the bandwidths of the forbidden and allowed frequencies, as a function of the generation number n, up to the 12th generation of the Fibonacci sequence, considering $k_x d_A=0.25$. This means a unit cell with 89 building blocks A and 144 building blocks B,
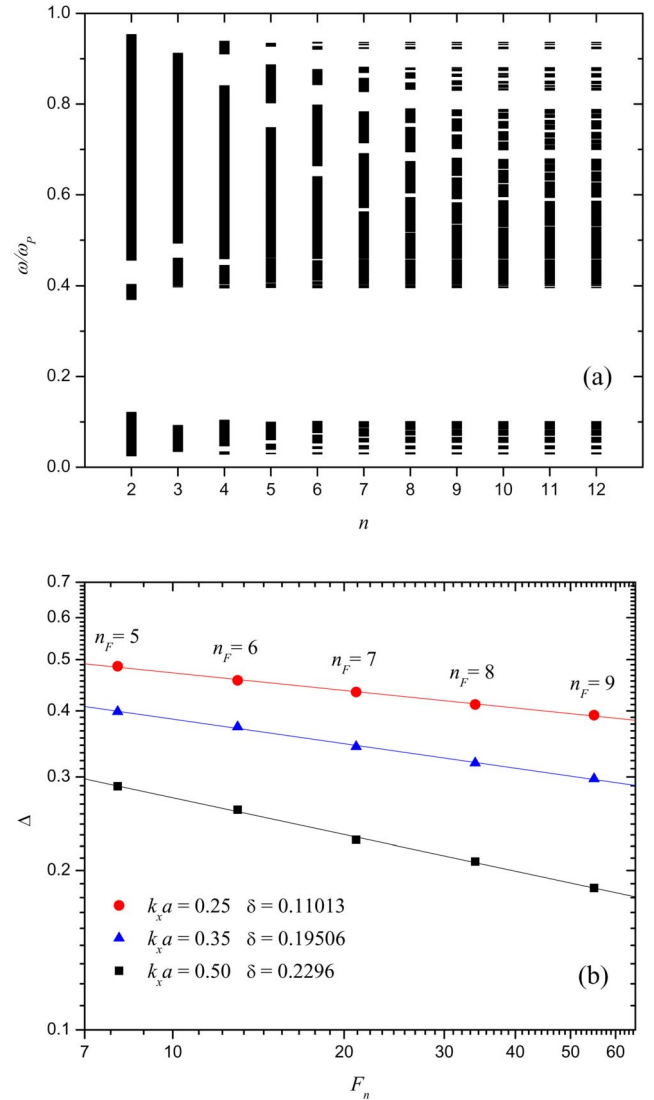
FIG. 5. (Color online) Localization and scaling properties in the Fibonacci quasiperiodic structure: (a) the distribution of bandwidths as a function of the generation number n and (b) log-log plot of the total width Δ of the passband regions against the Fibonacci number (the red, blue, and black lines correspond to the common dimensionless in-plane wave vector $k_x d_A$ equal to 0.25, 0.35, and 0.50, respectively).

totaling 233 building blocks. Note that, as expected, for large n, the allowed band regions get narrower and narrower as an indication of more localized modes. In fact, the total width Δ of the passband energy regions, which is the Lebesgue measure of the energy spectrum,[36] decreases with n as the power law $\Delta \sim F_n^{-\delta}$. Here, the exponent δ (the diffusion constant of the spectra) is a function of the common in-plane wave vector $k_x d_A$. This exponent can indicate the degree of localization of the excitation.[37] In Fig. 5(b), we show a log-log plot of these power laws for three different values of $k_x d_A$, namely, 0.25, 0.35, and 0.50.

The distribution of the bandwidths for the Thue-Morse structure, considering $k_x d_A=0.25$, is described in Fig. 6(a) up to the eighth generation of the sequence. The total passband
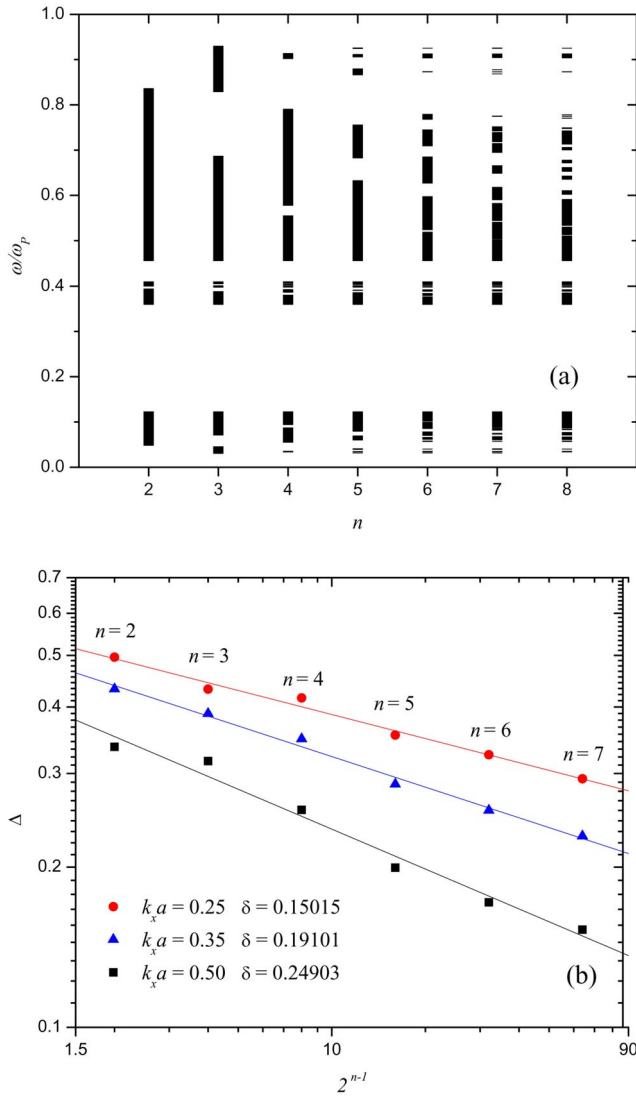
FIG. 6. (Color online) Same as in Fig. 5, but for the Thue-Morse quasiperiodic sequence (the red, blue, and black lines correspond to the common dimensionless in-plane wave vector $k_x d_A$ equal to 0.25, 0.35, and 0.50, respectively).
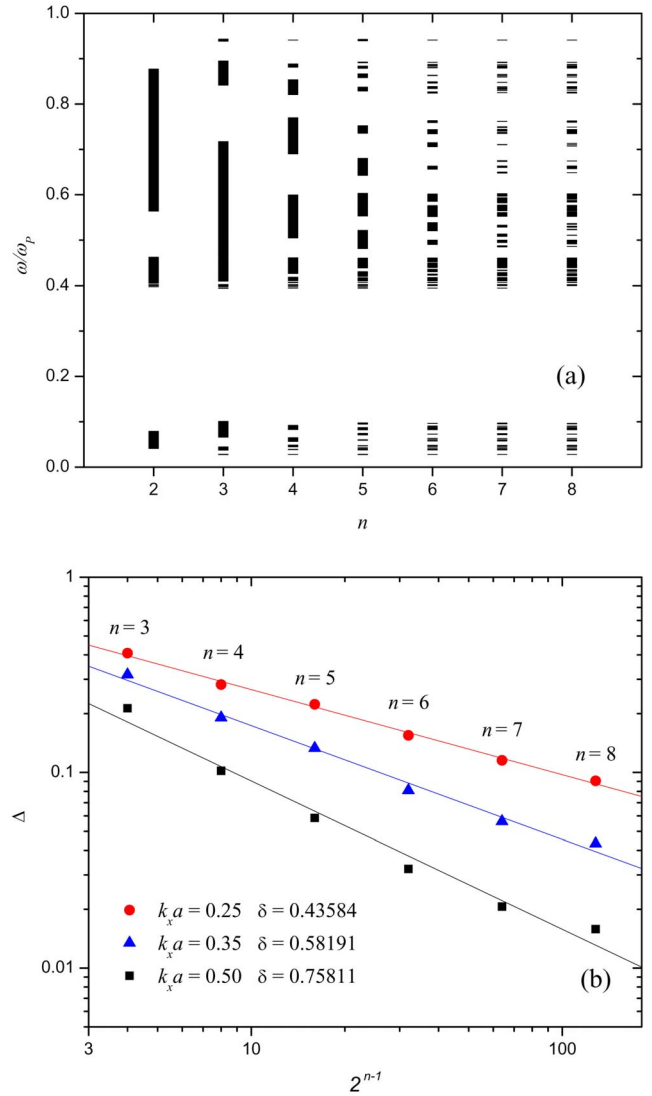

FIG. 7. (Color online) Same as in Fig. 5, but for the double-period quasiperiodic sequence (the red, blue, and black lines correspond to the common dimensionless in-plane wave vector $k_x d_A$ equal to 0.25, 0.35, and 0.50, respectively).

width has a different scale law, as compared to the Fibonacci case, namely, $\Delta \sim (2^{n-1})^{-\delta}$, as depicted in Fig. 6(b). A similar behavior was found for the double-period case, shown in Figs. 7(a) and 7(b).

We also investigated the multifractal distribution of the allowed frequencies. In order to characterize this distribution, it is convenient to introduce the function $f(\alpha)$, known as *multifractal spectrum* or *spectrum of scaling indices*. Loosely, one may think of the multifractal as an interwoven set of fractals of different dimensions $f(\alpha)$, where α is a measure of their relative strength.[38,39] The formalism relies on the fact that highly nonuniform probability distributions arise from the nonuniformity of the system. Usually, the singularity spectrum has a paraboliclike shape, distributed in a finite range $[\alpha_{min}, \alpha_{max}]$, which are the minimum and maximum singularity strengths of the intensity measure, respectively. They correspond also to the exponents governing the

scaling behavior in the most concentrated and rarefied regions of the frequency spectrum. The value of the $\Delta\alpha = \alpha_{max} - \alpha_{min}$ may be used as a parameter to measure the degree of randomness of the bandwidth distribution and, consequently, the degree of localization of the frequency spectrum. Figure 8 shows the $f(\alpha)$ functions for three different values of $k_x d_A$, namely, 0.25, 0.35, and 0.5, respectively, for the quasiperiodic structures considered in this work. In Fig. 8(a), we present $f(\alpha)$ for the 11th generation of the Fibonacci quasiperiodic sequence, whose unit cell is composed by 55 building blocks A and 89 building blocks B. Figure 8(b) [Fig. 8(c)] shows the $f(\alpha)$ for the eighth generation of the Thue-Morse (double-period) superlattice, whose unit cell is composed by 128 (161) building blocks A and 128 (85) building blocks B. The above multifractal analysis revealed a smooth $f(\alpha)$ function distributed in a finite range $[\alpha_{min}, \alpha_{max}]$ for all the quasiperiodic structures, with a summit at $f(\alpha_0) = 1$ for
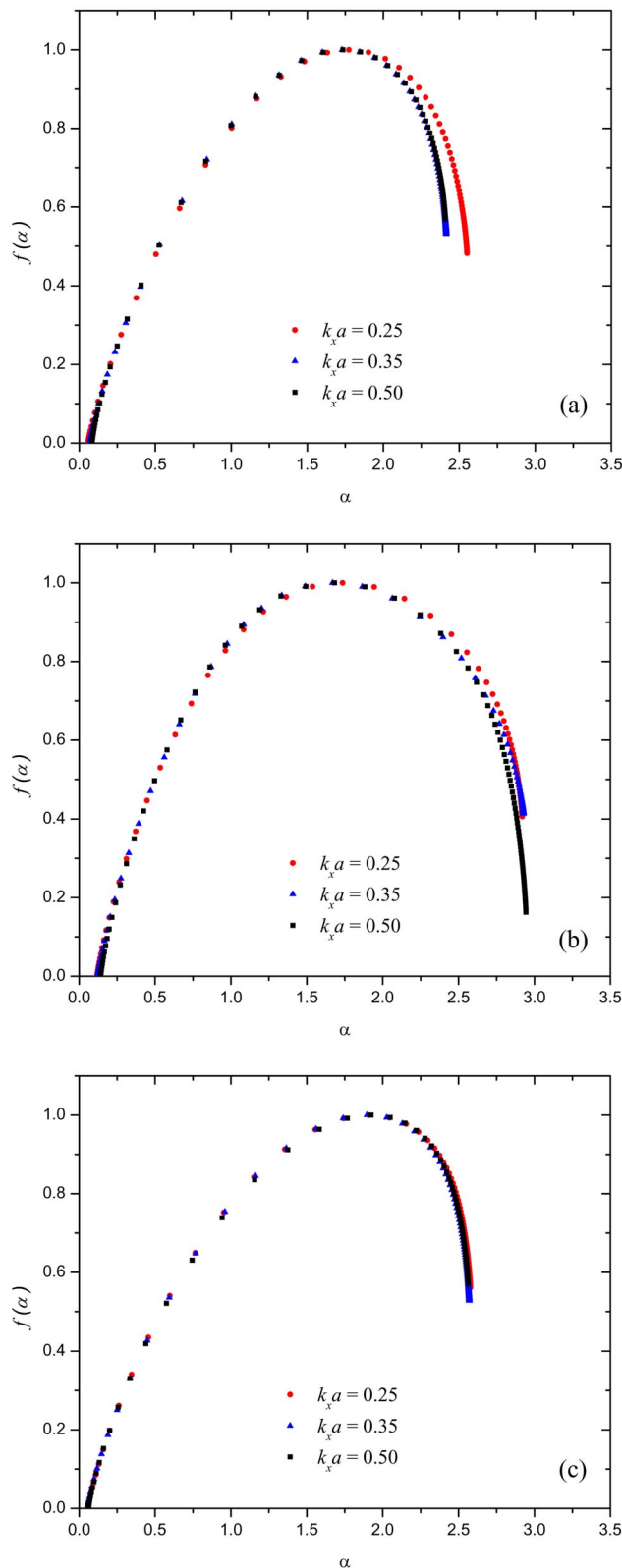
FIG. 8. (Color online) The $f(\alpha)$ functions of the photonic band gap bandwidths for the three quasiperiodic structures treated here. The values of $k_x d_A$ are given in the legend (a) Fibonacci, (b) Thue-Morse, (c) double period. (the red, blue, and black lines correspond to the common dimensionless in-plane wave vector $k_x d_A$ equal to 0.25, 0.35, and 0.50, respectively).

some value α_0 of α. These investigations clearly demonstrate that all the spectra correspond to highly nonuniform intensity distributions, and therefore, they possess the scaling properties of a multifractal.

IV. CONCLUSIONS

In this work, we presented a general theory for the propagation of plasmon-polaritons in periodic and quasiperiodic superlattices, in which one of the layers has negative refractive index (metamaterial), with simultaneously negative permittivity ϵ and permeability μ in the same frequency region. The spectra are illustrated in Figs. 2 (periodic superlattice) and 3 (three types of quasiperiodic structures). In both cases, we have observed that the effects of the introduction of the negative refractive index material in the spectra are more accentuated in the region $0.276 \leqslant \omega/\omega_p \leqslant 1.0$, where many bulk and surfaces modes exist with backward behavior, which is a typical property of metamaterials. On the other hand, in the interval $0 \leqslant \omega/\omega_p \leqslant 0.276$, we have only forward modes that are typical of positive refractive index materials. From these results, we can conclude that the photonic band gap spectrum presents properties for both positive and negative refractive index materials in an interval out of the range where the refractive index of the metamaterial is negative, i.e., $0.4 \leqslant \omega/\omega_p \leqslant 0.6$. This is a quite interesting property, not explored in a recent article,[40] where we studied the transmission spectra for the quasiperiodic sequences studied here.

We have also studied some physical properties of these substitutional sequences, mainly those related with their localization, as expressed by the distribution of bandwidths shown in Figs. 5(a), 6(a), and 7(a). Their self-similarity behavior was better described through the fractal and/or multifractal profiles, whose power laws were depicted in Figs. 5(b), 6(b), and 7(b), with no counterpart for the periodic case.

The most important experimental techniques to probe these spectra are the Raman light scattering and attenuated total reflection (ATR). In the case of Raman scattering, one uses a grating spectrometer to detect and analyze the scattered light. The typical shift of the frequency of the scattered light is in the range 0.6–500 meV, which makes this technique very appropriate for probing the plasmon-polariton spectra. On the other hand, ATR spectroscopy is much easier to deal with than the Raman one, but typically, it gives less precise results. However, it has been employed with success in a number of experiments for ordinary materials (cf. Ref. 41), including an interface between vacuum and a metamaterial slab.[42]

[1] V. G. Veselago, Sov. Phys. Usp. **10**, 509 (1968).

[2] S. Foteinopoulou, E. N. Economou, and C. M. Soukoulis, Phys. Rev. Lett. **90**, 107402 (2003); E. Cubukcu, K. Aydin, E. Ozbay, S. Foteinopoulou, and C. M. Soukoulis, Nature (London) **423**, 604 (2003).

[3] S. A. Ramakrishna, Rep. Prog. Phys. **68**, 449 (2005).

[4] J. B. Pendry, A. Holden, D. J. Robbins, and W. J. Stewart, IEEE Trans. Microwave Theory Tech. **47**, 2075 (1999).

[5] J. B. Pendry, Phys. Rev. Lett. **85**, 3966 (2000).

[6] J. B. Pendry, Science **306**, 1353 (2004).

[7] D. R. Smith, W. J. Padilla, D. C. Vier, S. C. Nemat-Nasser, and S. Schultz, Phys. Rev. Lett. **84**, 4184 (2000).

[8] D. R. Smith, J. B. Pendry, and M. C. K. Wiltshire, Science **305**, 788 (2004).

[9] R. A. Shelby, D. R. Smith, and S. Shultz, Science **292**, 77 (2001).

[10] C. G. Parazzoli, R. B. Greegor, K. Li, B. E. C. Koltenbah, and M. Tanielian, Phys. Rev. Lett. **90**, 107401 (2003).

[11] E. Yablonovitch, Phys. Rev. Lett. **58**, 2059 (1987).

[12] S. John, Phys. Rev. Lett. **58**, 2486 (1987).

[13] S. Johnson and J. D. Joannopoulos, *Photonic Crystals: The Road from Theory to Practice* (Kluwer, Boston, 2002).

[14] P. Yeh, A. Yariv, and C.-S. Hong, J. Opt. Soc. Am. **67**, 423 (1977).

[15] P. Yeh, *Optical Waves in Layered Media* (Wiley, New York, 1988).

[16] J. A. Gaspar-Armenta, F. Villa, and T. López-Ríos, Opt. Commun. **216**, 379 (2003).

[17] H. Jiang, H. Chen, H. Li, and Y. Zhang, Appl. Phys. Lett. **83**, 5386 (2003).

[18] H. Daninthe, S. Foteinopoulou, and C. M. Soukoulis, Photonics Nanostruct. Fundam. Appl. **4**, 123 (2006).

[19] A. Namdar, I. V. Shadrivov, and Y. S. Kivshar, Appl. Phys. Lett. **89**, 114104 (2006).

[20] S. B. Cavalcanti, M. de Dios–Leyva, E. Reyes-Gómez, and L. E. Oliveira, Phys. Rev. B **74**, 153102 (2006).

[21] R. Loudon, Adv. Phys. **13**, 423 (1964).

[22] *Polaritons*, edited by E. Burstein and F. de Martini (Pergamon, Oxford, 1974).

[23] D. L. Mills and E. Burstein, Rep. Prog. Phys. **37**, 817 (1974).

[24] C. H. Henry and J. J. Hopfield, Phys. Rev. Lett. **15**, 964 (1965).

[25] Z. Sun and H. K. Kima, Appl. Phys. Lett. **85**, 642 (2004).

[26] E. L. Albuquerque and M. G. Cottam, *Polaritons in Periodic and Quasiperiodic Structures* (Elsevier, Amsterdam, 2004).

[27] E. L. Albuquerque and M. G. Cottam, Phys. Rep. **376**, 225 (2003).

[28] H. V. Shadrivov, A. A. Sukhorukov, and Y. S. Kivshar, Appl. Phys. Lett. **82**, 3820 (2003).

[29] B. Djafari-Rouhani, L. Dobrzynski, O. Hardouin Duparc, R. E. Camley, and A. A. Maradudin, Phys. Rev. B **28**, 1711 (1983); R. E. Camley and D. L. Mills, *ibid.* **29**, 1695 (1984).

[30] G. F. Giuliani and J. J. Quinn, Phys. Rev. Lett. **51**, 919 (1983); W. Liu, G. Eliasson, and J. J. Quinn, Solid State Commun. **55**, 533 (1985).

[31] M. S. Vasconcelos and E. L. Albuquerque, Phys. Rev. B **57**, 2826 (1998).

[32] X. Jiang, Y. Zhang, S. Feng, K. C. Huang, Y. Yi, and J. D. Joannopoulos, Appl. Phys. Lett. **86**, 201110 (2005).

[33] I. S. Nefedov and S. A. Tretyakov, Phys. Rev. E **66**, 036611 (2002).

[34] L. Wu, S. He, and L. Shen, Phys. Rev. B **67**, 235103 (2003).

[35] N. C. Panoiu, R. M. Osgood, Jr., S. Zhang, and S. R. J. Brueck, J. Opt. Soc. Am. B **23**, 506 (2006).

[36] E. Maciá, Rep. Prog. Phys. **69**, 397 (2006), and references therein.

[37] P. Hawrylak and J. J. Quinn, Phys. Rev. Lett. **57**, 380 (1986).

[38] I. Procaccia, Proceedings of Nobel Symposium on Chaos and Related Problems [Phys. Scr., T **T9**, 40 (1985)].

[39] T. C. Halsey, P. Meakin, and I. Procaccia, Phys. Rev. Lett. **56**, 854 (1986).

[40] F. F. de Medeiros, E. L. Albuquerque, and M. S. Vasconcelos, J. Phys.: Condens. Matter **18**, 8737 (2006).

[41] N. Raj and D. R. Tilley, in *The Dielectric Function of Condensed Systems*, edited by L. V. Keldysh, D. A. Kirzhnitz, and A. A. Maradudin (North-Holland, Amsterdam, 1989).

[42] J. N. Gollub, D. R. Smith, D. C. Vier, T. Perram, and J. J. Mock, Phys. Rev. B **71**, 195402 (2005).